Rydberg blockade in a hot atomic beam

S. Yoshida,[1] J. Burgdörfer,[1] X. Zhang,[2] and F. B. Dunning[2]
[1]*Institute for Theoretical Physics, Vienna University of Technology, 1040 Vienna, Austria, EU*
[2]*Department of Physics and Astronomy, Rice University, Houston, Texas 77005-1892, USA*
(Received 2 November 2016; revised manuscript received 14 February 2017; published 11 April 2017)

The dipole blockade of very-high-n, $n \sim 300$, strontium $5snf\ ^1F_3$ Rydberg atoms in a hot atomic beam is studied. For such high n, the blockade radius can exceed the linear dimensions of the excitation volume. Rydberg atoms formed inside the excitation volume can, upon leaving the region, continue to suppress excitation until they have moved farther away than the blockade radius. Moreover, the high density of states originating from the many magnetic sublevels associated with the F states results in a small but finite probability of excitation of $L = 3$ $n\ ^1F_3$ atom pairs at small internuclear separations below the blockade radius. We demonstrate that these effects can be distinguished from one another by the distinct features they imprint on the Mandel Q parameter as a function of the duration of the exciting laser.

DOI: 10.1103/PhysRevA.95.042705

I. INTRODUCTION

For a dilute gas the interaction between ground-state atoms is small. However, the interactions between atoms can be dramatically enhanced by exciting them to high-n Rydberg states. In particular, resonant excitation of one atom can shift the energy of neighboring atoms preventing their subsequent excitation by photons of the same frequency and leading to dipole blockade [1,2]. Blockade effects limit the number of Rydberg atoms that can be excited within a given volume and can facilitate the formation of strongly correlated many-body systems allowing the generation of entanglement between neighboring atoms [3–5], the realization of quantum gates [6–8], and the observation of many-body Rabi oscillations [9,10]. The strengths of such interactions increase rapidly with principal quantum number n. In the presence of a weak electric field, degenerate high-L states can form, through their superpositions, strongly polarized states with large dipole moments $\langle d \rangle \propto n^2$. In contrast, the induced dipole moments for (nondegenerate) low-L states are smaller and increase with applied field, $\langle d \rangle \sim \alpha F$, where F is the field strength and $\alpha \propto n^7$ is the polarizability. For Rydberg atom pairs this difference in the single-atom response to a perturbing field F leads, within a perturbative approach, to the dipole-dipole interaction C_3/R^3, with $C_3 \propto n^4$, for degenerate high-L states, and to the van der Waals interaction C_6/R^6, with $C_6 \propto n^{11}$, for low-L states, where R is the internuclear separation.

Blockade effects have been studied experimentally using a number of low-L, s, p, and d alkali-metal Rydberg states with values of $n \lesssim 100$ [1,2,11–13], resulting in blockade radii up to a few micrometers. Measurements have recently been extended to $n \sim 300$ using $5snf\ ^1F_3$ strontium Rydberg states [14]. Due to its strong n scaling, the van der Waals pair interaction becomes quite strong for $n \sim 300$. Moreover, because of their small quantum defects $\delta_F \sim 0.089$, strontium $^1F_3$ states are nearly degenerate with the neighboring manifold of high-L states. This not only further enhances interactions but also leads to strong mixing with higher-L states modifying the oscillator strength of the interacting pair eigenstate. The large energy shift and the suppression of oscillator strength result in a blockade radius R_B as large as ∼0.1 mm (see Sec. III B). In consequence, it is possible to study blockade effects where R_B exceeds the linear dimension of the excitation volume. Similar situations have been achieved using ultracold atoms by reducing the size of the atom cloud [10,15,16]. Moreover, the high photoexcitation rates achieved for $^1F_3$ states allow the observation of blockade effects in a hot atomic beam of relatively low density $\rho_V \sim 10^9$ cm^{-3} [14]. The motion of atoms into and out of the excitation volume gives rise to features in Rydberg blockade not seen using ultracold trapped atom ensembles. At the same time, the very high density of states near $n \simeq 300$ results in highly complex quasimolecular energy level diagrams and in small, but finite, oscillator strengths for excitation near resonance under conditions where blockade might otherwise be expected. In this work we explore both experimentally and theoretically the effects of atomic motion in a hot beam and of the high density of states for very high $n \gtrsim 300$ levels on Rydberg blockade and its partial suppression. We show that these effects give rise to distinct signatures in the time dependence of the Mandel Q parameter [17] characterizing the correlated multiple-atom excitation allowing each to be distinguished.

The structure of this paper is as follows. In Sec. II we briefly sketch the experimental approach. In Sec. III we present a detailed theoretical analysis of Rydberg pair interactions for very-high-n levels, in particular for the $n\ ^1F_3$ levels in strontium, the preliminary results of which were discussed in [14]. In Sec. IV we extend this work and consider the effects of atomic motion on the Rydberg excitation dynamics. The comparison between experimental and theoretical results is discussed in Sec. V, followed by concluding remarks in Sec. VI.

II. EXPERIMENTAL APPROACH

The present apparatus is shown schematically in Fig. 1 and was developed from that used in earlier experiments in the same laboratory. Strontium atoms contained in a tightly collimated beam are excited in near-zero field to selected high-n $n\ ^1F_3$ states near the center of an interaction region defined by three pairs of copper electrodes. The number of Rydberg atoms created is determined using field ionization, the product electrons being detected using a microchannel plate (MCP).

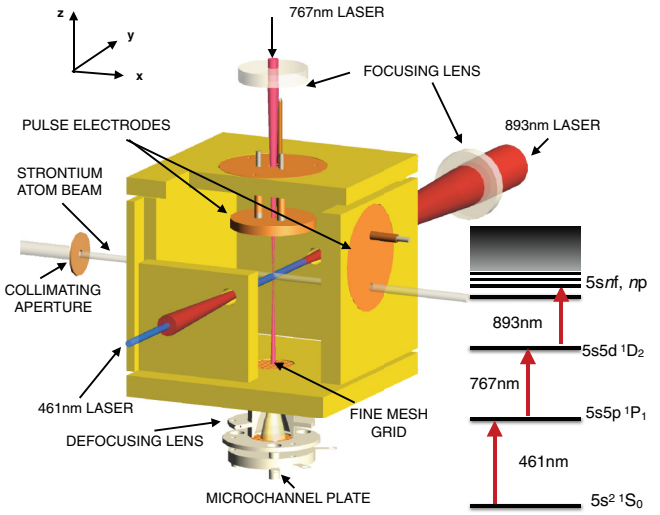

FIG. 1. Schematic diagram of the apparatus. The inset shows the excitation scheme employed.

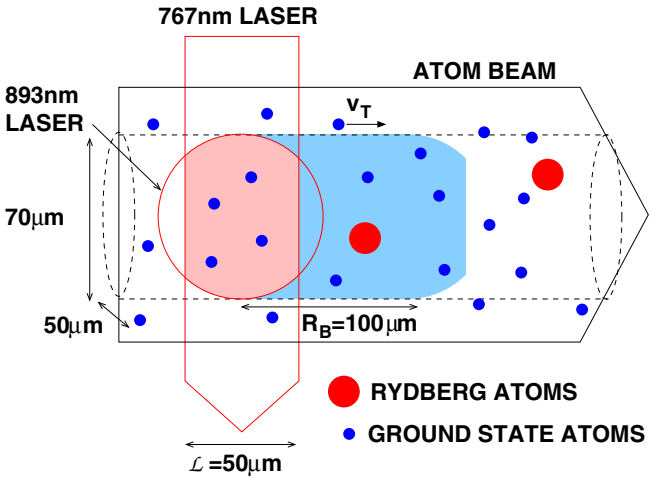

FIG. 2. Schematic diagram of the Rydberg blockade in a hot atomic beam. Rydberg atoms are excited in the volume defined by the intersection of the 767- and 893-nm laser beams (excitation region shaded in light red), but can continue to suppress further excitation until they have moved a distance $\sim R_B$ (shaded in light blue) from the excitation region. In the numerical studies, only the atoms inside the elliptically shaped cylinder (dashed line) are simulated.

The strontium atom beam is provided by a cylindrical oven that is positioned inside a water-cooled enclosure. The atom beam exits the oven through a short 500-μm-diam canal and is further collimated using a 500-μm-diam aperture located near the entrance to the differentially pumped interaction region, resulting in a beam with a divergence of $\theta_{\rm div} \simeq 4$ mrad full width at half maximum (FWHM). The temperature of the oven is monitored by thermocouples attached to its front and rear faces. (The nose of the oven is operated $\sim$40 °C hotter than the back to prevent blocking of the exit canal.) The average of these values is used when estimating the strontium vapor pressure in the oven. The oven can be operated at temperatures up to $T \sim 650$ °C, sufficient to produce estimated beam densities of $\sim 10^9$ cm^{-3} in the excitation region. The most probable (longitudinal) velocities of atoms in the beam lie in the range $v_T \sim$ (4–5) $\times 10^2$ m s^{-1}.

The three-photon excitation scheme employed is shown in the inset in Fig. 1 and utilizes the $5s5p\ ^1P_1$ and $5s5d\ ^1D_2$ intermediate states and radiation at 461, 767, and 893 nm. (The decay rates associated with the $5s5d\ ^1D_2 \rightarrow 5s6p\ ^1P_1$ and $5s5p\ ^1P_1 \rightarrow 5s4d\ ^1D_2$ transitions are small and population transfer to these states is unimportant on the less than 1 μs time scale of the present experiments.) The advantage of using three-photon excitation is that powers of up to $\sim$1.2 W can be readily obtained to excite the final transition to the Rydberg state resulting in high photoexcitation rates. The required radiation is provided by diode laser systems whose output wavelengths are stabilized using Fabry-Pérot transfer cavities locked to a polarization-stabilized helium-neon laser. The 461- and 893-nm beams are linearly polarized along the z axis indicated in Fig. 1 and the 767-nm beam is polarized along the y axis, leading to creation of the superposition $|nF, M = 1\rangle + |nF, M = -1\rangle$. The crossed 767- and 893-nm beams are focused at the center of the interaction region to $1/e^2$ diameters of $\sim$50 and 70 μm, respectively, resulting in a strongly localized excitation volume of $\sim 1.3 \times 10^{-7}$ cm^3 that typically contains tens to hundreds of ground-state atoms (see Fig. 2). The 461-nm laser is not focused. Both the 461- and 767-nm lasers are tuned on resonance. The linear dimension of the excitation volume ($\lesssim$70 μm) is smaller than the Rydberg blockade radius $R_B \simeq 100$ μm for the present system (Fig. 2; see also below). Therefore, atoms that have escaped from the excitation volume may also contribute to blockading further excitation while they remain close to the excitation volume.

Stray fields in the excitation volume are minimized by application of small offset potentials to the electrodes that define the interaction region. These potentials are optimized by observing the widths of the $n\ ^1F_3$ features in the Rydberg excitation spectra, which are very sensitive to the presence of stray fields, and systematically varying the offsets to minimize their widths. As illustrated in Fig. 3, once this process is complete, well-resolved Rydberg excitation spectra can be obtained even for values of $n > 500$. Given that the Stark crossing field, $1/(3n^5)$ a.u., at $n = 520$ is only $\sim$40 μV cm^{-1} and that the Stark broadening is sufficiently small that the P and F states remain well resolved, the data indicate that stray fields in the excitation volume are reduced to values less than 10 μV cm^{-1}. These are significantly smaller than seen in our earlier work [18], presumably because the excitation volume is smaller, which diminishes the effect of stray field inhomogeneities. The overall experimental linewidth, $\sim$8 MHz at $n \sim 310$, is attributed to transit time broadening, Doppler effects, and fluctuations in laser wavelengths.

Measurements are conducted in a pulsed mode. The output of the 461-nm laser is chopped into a series of pulses with a pulse repetition frequency of $\sim$20 kHz using an acousto-optic modulator (AOM). The other beams remain on at all times. By varying the 461-nm pulse duration, the blockade effects in the time evolution of Rydberg excitation can be studied. The number of Rydberg atoms created is determined by selective field ionization, which is accomplished by generating a slowly increasing (rise time $\sim$2 μs) electric field by applying a linearly increasing voltage ramp to the lower electrode. Since the

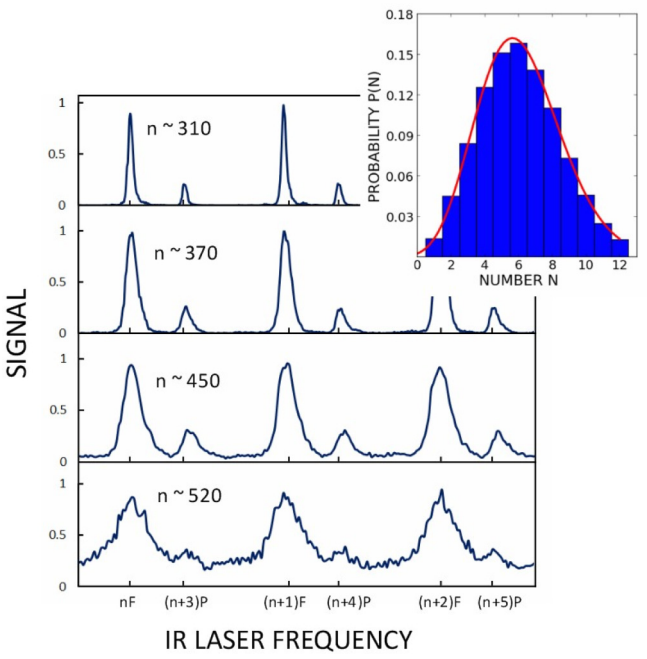

FIG. 3. Excitation spectra measured for $n \sim 310$, 370, 450, and 520. The various spectra are normalized to the same peak height. The frequency axis is scaled by n^{-3} so that the spacing between, say, the n and $n+1$ features in each spectrum is the same. The large and small peaks in the spectra correspond to excitation of $^1F_3$ and $^1P_1$ states, respectively. The inset shows a typical electron number distribution recorded using a large Rydberg atom production rate (see the text). For comparison, a Poissonian distribution having the same mean value is included.

time scale for a single experimental cycle is short, $\sim 10\ \mu$s, the Rydberg atoms typically travel only ~ 5 mm from their point of formation before being ionized. Product electrons exit the interaction region through a series of two 2-cm-diam $\sim 80\%$-transparent fine mesh grids and then enter a cylindrical lens that defocuses them before passing through a further grid to strike the MCP. The output pulses from the MCP are amplified and fed to a discriminator. Output pulses from the discriminator are used to generate discrete charge pulses for injection into a charge-sensitive amplifier whose output is fed to a multichannel analyzer to determine the number of electrons detected. Data are accumulated following many laser pulses to build up the electron number distribution. The probability that zero electrons are detected is determined by summing the number of events in which one, or more, electrons are detected and subtracting this sum from the total number of laser pulses used to acquire the data. The overall electron detection efficiency η could not be directly determined, but was inferred from the known grid transparencies and published MCP detection efficiencies. With the MCP operating with sufficient gain to saturate the count rate, the detection efficiency is estimated to be $\eta \simeq 0.51$.

To check the performance of the detection system at high count rates where nonlinearities might arise, tests were undertaken with the apparatus configured as in earlier studies with the 767- and 893-nm beams copropagating antiparallel to the 461-nm beam, which leads to a sizable increase in the excitation volume and in the Rydberg atom production rates. A typical distribution of the number N_R of electrons recorded at the MCP using low atom beam densities and relatively long, ~ 1-μs, laser pulses, i.e., recorded under conditions where Rydberg blockade effects are not expected, is shown as an inset in Fig. 3 and is well fit by a Poissonian distribution, demonstrating that sizable numbers of electrons can be detected without any significant nonlinearities in detection efficiency.

III. INTERACTIONS BETWEEN RYDBERG ATOMS

The determination of the Rydberg-Rydberg interaction strength both within and beyond the blockade radius requires use of a nonperturbative approach. The Hamiltonian for two interacting atoms is given within the Born-Oppenheimer approximation by

$$H = H_A + H_B + U_{\rm int}(R), \tag{1}$$

where $H_{A\,(B)}$ is the Hamiltonian of the isolated atoms A (B) and $U_{\rm int}(R)$ is the pair interaction between them. For distances R sufficiently large that there is no significant overlap between the electronic wave functions of the atoms, the interaction $U_{\rm int}(R)$ can be approximated using a multipole expansion, the leading terms of which are given by

$$U_{\rm int}(R) \simeq U_{dd}(R) + U_{dq}(R) + U_{qq}(R), \tag{2}$$

where $U_{dd}(R)$ denotes the dipole-dipole interaction, $U_{dq}(R)$ the dipole-quadrupole interaction, and $U_{qq}(R)$ the quadrupole-quadrupole interaction. Given the large blockade radius R_B for high-n Rydberg atoms, the multipole expansion [Eq. (2)] applies not only for $R > R_B$ but also for R considerably smaller than R_B, $R \gtrsim R_B/3$ (see below).

For the matrix representation of the quasimolecular Hamiltonian [Eq. (1)] we employ a basis $|n_A, L_A, M_A; n_B, L_B, M_B\rangle$ formed by the product states of two noninteracting many-electron atoms. By numerically diagonalizing the Hamiltonian, the energy shifts associated with the multipole terms are evaluated nonperturbatively. One challenge in such calculations is the accurate representation of the wave functions $|n, L, M\rangle$ for an isolated many-electron atom. For Rydberg atoms with one electron far outside the ionic core, a convenient starting point is the single-active-electron (SAE) model [19], in which the effective binding potential generated by the $N_e - 1$ electron core for the Rydberg electron is chosen such as to yield the measured quantum defects δ_L, i.e., the phase shifts associated with core scattering for isolated atoms. The resulting Rydberg wave functions are typically quite accurate outside the core region. Since the multipole moments of Rydberg states are rather insensitive to the details of the wave functions near the core, a single-active-electron model can be used to evaluate the energy shifts quite accurately, in particular for states well removed from perturbers [20]. A more accurate treatment for alkaline-earth atoms involves the two-active-electron (TAE) model [21,22], in which the Hamiltonian of the two valence electrons outside the ionic core is numerically diagonalized and the model potential now accounts for the influence of the $N_e - 2$ electrons in the closed ionic shell. In order to simulate both the dipole transition strengths involved in the present excitation scheme and the

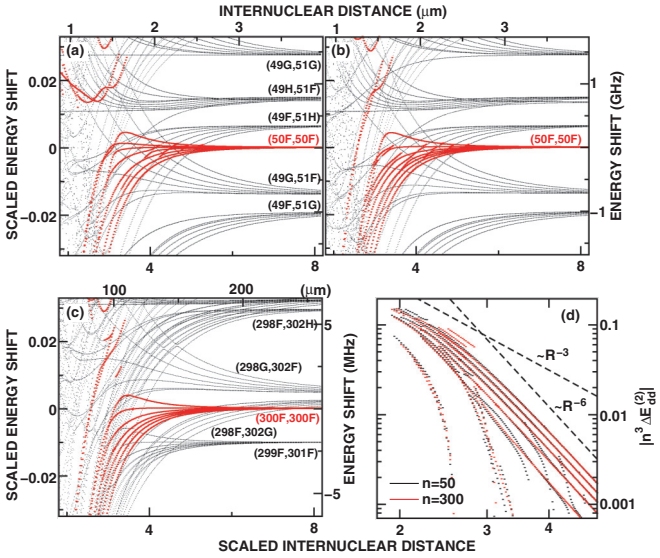

FIG. 4. Energy levels for Rydberg atom pairs with $\Lambda_M = M_A + M_B = 0$ near the $|nF;nF\rangle$ pair for $n = 50$ calculated using (a) a TAE model and (b) an SAE model and (c) for $n = 300$ using an SAE model. The eigenstates with more than 10% probability when projected onto the noninteracting pair of nF states are highlighted in red. For these, the states with $\Delta E_{dd}^{(2)} < 0$ are plotted on a log-log scale in (d) (black, $n = 50$; red, $n = 300$). In the calculations, the basis states are limited to quantum numbers with $n \in [n-2, n+2]$, $L \leqslant 5$, and $|M| \leqslant 5$. Both atoms are aligned along the z axis. The internuclear separation R is scaled by $n^{7/3}$ and the energy shift by n^{-3} (see the text). Dashed lines indicate different power laws.

positions of all relevant energy levels near $n \sim 300$ $^1F_3$ states the two methods are combined. With the model potential used in the SAE model adjusted to yield the same quantum defect as obtained from the TAE model, the energy levels calculated using both approaches agree well. The close agreement between predictions made using the TAE and SAE models for the quasimolecular energy levels of a Rydberg atom pair is illustrated in Figs. 4(a) and 4(b) for a moderate n value $n = 50$, where both models can be readily applied. Only at small R, well inside the blockade radius, do minor differences become noticeable. Given the accurate wave functions for both low- and high-n Rydberg states provided by the TAE model, this model is employed to determine the n dependence of the excitation strength for creating a pair of Rydberg atoms utilizing the $5s5d$ intermediate state, which is crucial when analyzing the blockade probability. However, the computation times required using the TAE model increase rapidly with n limiting calculations to values of $n \lesssim 100$. Therefore, n scaling is employed to extrapolate calculations undertaken at low n to the higher values, $n \simeq 300$, studied experimentally.

A. n scaling in the Rydberg-Rydberg interaction

Extrapolation of the Rydberg pair energies from $n = 50$ to very high $n > 300$ requires n scaling and a transformation to reduced distance and energy scales for which the energy diagrams becomes approximately scaling invariant. This method combines atomic Coulomb scaling with scaling of the interatomic potential assuming that the interaction obeys a monomial power law $\sim R^{-k}$ with power k. Deviations from strict scaling invariance are expected if the interaction is polynomial rather than monomial as is the case for the multipole expansion in Eq. (2). However, approximate scaling invariance is expected when one term of the expansion (usually with the lowest power k) dominates.

We first analyze the n scaling of the dipole-dipole interaction $U_{dd}(R)$, which provides the dominant contribution to Eq. (2) before considering the scaling of the higher-order multipoles. To illustrate the n scaling of $U_{dd}(R)$, we consider a simplified model in which the target pair state $|n,L;n,L\rangle$ (i.e., both atoms occupy the same state, $n_A = n_B = n$ and $L_A = L_B = L$) is coupled only to a single other pair state $|n',L';n'',L''\rangle$. The matrix representation of the energy shift $\Delta H = H - E_{nL;nL}$ from the target pair in this two-pair state subspace then reads

$$\Delta H^{(2)} = \begin{pmatrix} 0 & W \\ W & E_{n'L';n''L''} - E_{nL;nL} \end{pmatrix}. \tag{3}$$

Here W is the coupling matrix element with the R dependence

$$W = \langle n',L';n'',L''|U_{dd}(R)|n,L;n,L\rangle \simeq \frac{n^4 W_0}{R^3} \tag{4}$$

explicitly displaying the power law $k = 3$ and the n dependence. The energy difference between the pair states exhibits the atomic Coulomb scaling

$$E_{n'L';n''L''} - E_{nL;nL} \simeq \frac{1}{n^3}[(n' + n'' - 2n) - (\delta_{L'} + \delta_{L''} - 2\delta_L)] \equiv \frac{\delta E_0}{n^3}, \tag{5}$$

where δ_L is the quantum defect for L states (unless otherwise noted, atomic units are used throughout). By scaling the internuclear distance as $R = R_0 n^{7/3}$ [14], the dipole-dipole coupling scales [Eq. (4)] as $W = n^{-3} W_0/R_0^3$. Correspondingly, the n-dependent part of the Hamiltonian can be factorized out, i.e.,

$$\Delta H^{(2)} = n^{-3} \begin{pmatrix} 0 & W_0/R_0^3 \\ W_0/R_0^3 & \delta E_0 \end{pmatrix} = \Delta H_0^{(2)} n^{-3}, \tag{6}$$

indicating that the energy shifts of pair states, i.e., the eigenenergies of $\Delta H^{(2)}$, become invariant by scaling with n^{-3}. The eigenvalues of the scaled energy shift $\Delta H_0^{(2)}$ are evaluated as

$$(E_0)_{1,2} = \frac{1}{2}\left(\delta E_0 \pm \sqrt{\delta E_0^2 + \frac{4W_0^2}{R_0^6}}\right). \tag{7}$$

When $|\delta E_0| \ll |W_0/R_0^3|$ (i.e., when the two pairs are nearly degenerate),

$$(E_0)_{1,2} \simeq \frac{1}{2}\delta E_0 \pm \frac{W_0}{R_0^3}, \tag{8}$$

exhibiting the dipole-dipole splitting. This implies that the superpositions $|n,L;n,L\rangle \pm |n',L';n'',L''\rangle$ form polarized pairs of atoms having the eigenenergies $\pm W_0/R_0^3$, respectively. They are perturbed by the small energy difference δE_0. The formation of polarized pair states typically occurs for pairs of degenerate L states with vanishingly small quantum defects

($L > 3$ for strontium). In the opposite limit of weak coupling between the pairs $|\delta E_0| \gg |W_0/R_0^3|$ (for example, for a pair of low-L states), the scaled eigenenergies

$$(E_0)_1 \simeq -\frac{1}{\delta E_0}\frac{W_0^2}{R_0^6}, \quad (E_0)_2 \simeq \delta E_0 + \frac{1}{\delta E_0}\frac{W_0^2}{R_0^6} \tag{9}$$

display energy shifts $\sim R_0^{-6}$ indicating van der Waals interactions. The above analysis can be extended to include multiple pair states coupled to the target pair as long as the energy difference scales as $E_{n'L';n''L''} - E_{nL;nL} \sim n^{-3}$ and the scaling invariance of the energy shift [Eq. (6)] associated with the dipole-dipole interaction U_{dd} can be identified. One prominent exception, however, is a Förster resonance [23] for which $\delta E_0 \simeq 0$ [Eq. (5)] and the Coulomb scaling $\sim n^{-3}$ of the energy difference is replaced by $\sim n^{-4}$, thereby breaking this form of scaling invariance.

For strontium $n\,^1F_3$ pair states, the scaling invariance of the energy shift associated with $U_{dd}(R)$ is demonstrated in Figs. 4(b) and 4(c), which show the energy diagram for pairs of interacting $n = 50$ and $n = 300$ Rydberg atoms calculated with a SAE model using only $U_{dd}(R)$. When scaled, quasimolecular energy levels adiabatically connecting to the $|n,F;n,F\rangle$ states behave nearly identically. For better visibility, pair states with more than 10% overlap with the noninteracting $|n,F;n,F\rangle$ state are highlighted in red. The subset of states that shift downward in energy are plotted on a log-log scale in Fig. 4(d) and quantitatively confirm the scaling invariance between $n = 50$ and $n = 300$. At large R the energy shifts display the R^{-6} dependence typical of the van der Waals interaction. The nearly degenerate limit $|W_0/R^3| \gg \delta E_0$ is reached near $R_0 = 3$ (or $R = 3n^{7/3}$ corresponding to 100 μm for $n = 300$) when the energy shift crosses over to an R^{-3} dependence, indicating the formation of a polarized pair state. This is due to the fact that the $n\,^1F_3$ pair state couples most strongly to the nearly degenerate $n\,^1G_4$ pair state, rendering the two-state model discussed above applicable.

The noticeable differences between the energy diagrams for $n = 50$ and 300 [Figs. 4(a) and 4(c)] directly reflect the breaking of scaling invariance. For example, the energy difference of the $|(n-1),F;(n+1),F\rangle$ pair state to the target $|n,F;n,F\rangle$ pair state yields $\delta E_0 = 0$ [Eq. (5)] and therefore the leading-order term in the energy difference scales as $1/n^4$ rather than $1/n^3$. In consequence, the relative position of $|(n-1),F;(n+1),F\rangle$ pair states with respect to the $|n,F;n,F\rangle$ states varies with n being closer for $n \sim 300$ than for $n \sim 50$. Another example is the $|(n-1),F;(n+1),H\rangle$ state that couples to the target pair state via the $|n,G;n,G\rangle$ pair state. Here the numerically calculated quantum defects happen to approximately fulfill the relation $\delta_G \simeq (\delta_F + \delta_H)/2$ also yielding $\delta E_0 = 0$ [Eq. (5)] and breaking the n^{-3} scaling. While for $n = 50$ the $|49F;51H\rangle$ and the $|50F;50F\rangle$ states undergo an avoided crossing near $R_0 \simeq 4$ resulting in a marked deviation from the R^{-6} behavior, for $n = 300$ the corresponding $|299F;301H\rangle$ state is found at much higher scaled energy outside the energy window covered by Fig. 4(d) and the corresponding avoided crossings are absent.

Contributions from higher-order multipoles with different $\sim R^{-k}$ dependences may also break the scaling invariance [24]. A matrix element of the dipole-quadrupole interaction

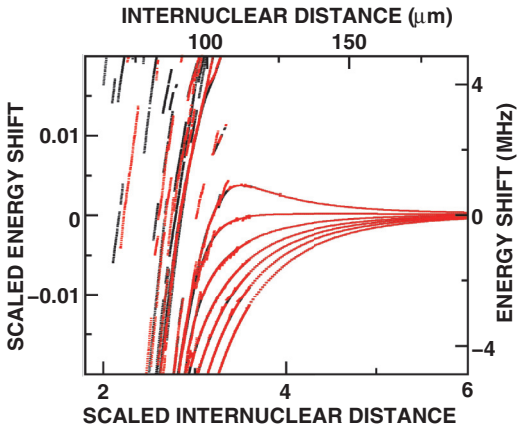

FIG. 5. Energy levels for Rydberg atom pairs with $\Lambda_M = M_A + M_B = 0$ when including only $U_{dd}(R)$ (shown in black) and including higher-order multipoles (shown in red). The plotted pair eigenstates have more than 12% probability for $U_{dd}(R)$ and 10% for higher-order multipoles when projected onto a noninteracting $n = 300$ $^1F_3$ pair state. In the asymptotic limit $R \to 0$, these eigenstates have an approximately good quantum number $L_{\text{total}} = |\vec{L}_A + \vec{L}_B|$ ($L_{\text{total}} = 0,1,\ldots,6$ from the lowest energy). The calculations are undertaken using an SAE model. The basis size is limited to $n \in [n-2, n+2]$, $L \leqslant 8$, and $|M| \leqslant 8$. Both atoms are aligned along the z axis. The internuclear separation R is scaled by $n^{7/3}$ and the energy shift by n^{-3}.

typically scales as

$$\langle n',L';n'',L''|U_{dq}(R)|n,L;n,L\rangle \propto \frac{n^6}{R^4} = n^{-10/3}\frac{1}{R_0^4} \tag{10}$$

and that of the quadrupole-quadrupole interaction as

$$\langle n',L';n'',L''|U_{qq}(R)|n,L;n,L\rangle \propto \frac{n^8}{R^5} = n^{-11/3}\frac{1}{R_0^5}. \tag{11}$$

Consequently, the ratio of the dipole-quadrupole corrections to the leading dipole-dipole interaction scales as $U_{dq}/U_{dd} \sim 1/(R_0 n^{1/3})$ and that of the quadrupole-quadrupole corrections as $U_{qq}/U_{dd} \sim 1/(R_0^2 n^{2/3})$. Higher-order multipole corrections are therefore expected to contribute only for small R_0 or n. To confirm this behavior, the pair eigenstates for $n = 300$ having significant overlap with noninteracting $n = 300$ $^1F_3$ pair states are plotted in Fig. 5 when including only the dipole-dipole interaction (in black) and when including the higher-order multipoles (in red). We note that in Fig. 5, due to the lower density of states when including only $U_{dd}(R)$, states with more than 12% overlap are plotted, whereas this is reduced to 10% overlap when including the high-order multipoles. The two calculations show little difference, in particular beyond $R_0 > 2.5$. Some deviations are visible at small R_0. However, these deviations do not affect the blockade probability for which the excitation strengths are integrated over the eigenstates within the laser linewidth. In the current experiments, the laser linewidth is $\sim 0.04 n^{-3} \simeq 8$ MHz. Since additional higher multipole terms decay even faster with n, we can conclude that for $n \sim 300$ all terms beyond the dipole-dipole interaction only play a significant role in the regime $R_0 < 2.5$. This observation has important implications for the n scaling: When TAE calculations for $n = 50$ are extrapolated to $n \gtrsim 300$, only the

dipole-dipole interaction should be scaled and corrections due to higher-order multipoles should be neglected. We note that in the simulations the matrix elements of U_{qq} are only evaluated among magnetic sublevels in degenerate manifolds to examine the dominant contributions, i.e., the first-order corrections due to quadrupole-quadrupole interactions.

B. Excitation strength of Rydberg pairs

The oscillator strengths for excitation of different eigenstates are laser-polarization dependent as this determines which M levels of the individual atoms that eventually form the Rydberg pair are produced. In the present work the intermediate $5s5d$ state is populated by two-photon excitation involving a 461-nm laser polarized along the z axis and a 767-nm laser polarized along the y axis yielding the superposition $|5D, M = 1\rangle + |5D, M = -1\rangle$. The 893-nm laser is polarized along the z axis and excites the final product Rydberg state $|nF, M = 1\rangle + |nF, M = -1\rangle$. When an $|n, F; n, F\rangle$ pair state is excited, it can thus have molecular quantum numbers Λ_L relative to the polarization axis $\hat{z}$ of the 893-nm laser, $\Lambda_L = M_A + M_B = 0, \pm 2$. This implies a coherent superposition of states with different projections of the angular momentum onto the internuclear axis Λ_R. The corresponding expansion coefficients are the rotation matrix elements $\mathcal{D}_{\Lambda_L \Lambda_R}(\theta)$, where θ is the angle between the laser polarization axis and the internuclear axis. These θ-dependent expansion coefficients lead to an angular dependence in the excitation strength of the molecular states [14]. Figures 6(a)–6(c) show excitation spectra for creating a $|70F; 70F\rangle$ atom pair from a $|5s5d\ ^1D_2; 5snf\ ^1F_3\rangle$ pair aligned along the x, y, and

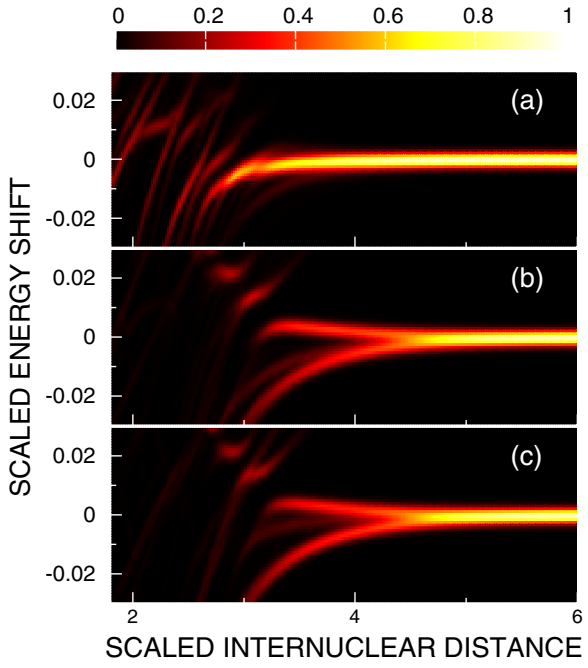

FIG. 6. Calculated excitation spectra for creation of Rydberg atom pairs as a function of internuclear separation R. Here R is scaled by $n^{7/3}$ and the detuning by n^{-3}. The laser linewidth is set to $0.002n^{-3}$. The atoms are assumed to be aligned along (a) the x axis, (b) the y axis, and (c) the z axis. The calculation are done for $n = 70$ and $L_{\max} = 8$.

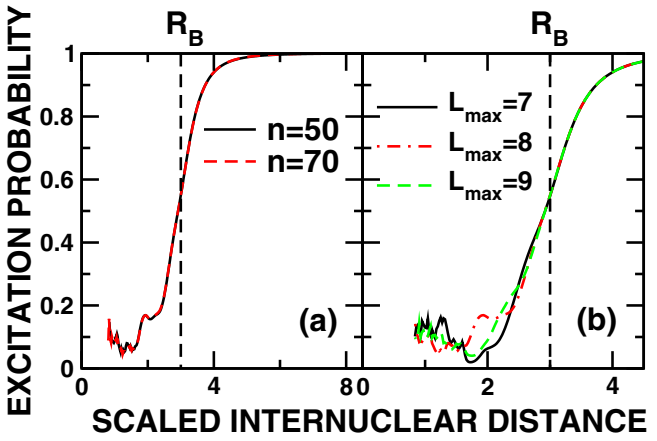

FIG. 7. Probability for excitation of a pair of interacting Rydberg states from the $|5s5d\ ^1D_2; 5snf\ ^1F_3\rangle$ pair state. The probability is calculated assuming that the 893-nm laser is tuned on resonance for a pair of noninteracting $5snf\ ^1F_3$ atoms and the linewidth is $0.04n^{-3}$. The results are averaged over atom pair orientations and are normalized to one in the limit $R \to \infty$. The calculations are undertaken using the TAE model. In (a) the results for $n = 50$ (black) and for $n = 70$ (red), both with $L_{\max} = 8$, are almost indistinguishable, confirming the scaling invariance. In (b) the results for $n = 50$ with different basis sizes (varying $L_{\max}$ from 7 to 9) are compared. The internuclear separation R is scaled by $n^{7/3}$.

z axes, respectively, calculated using the TAE model. The basis states for the TAE calculation are limited to quantum numbers with $n \in [n-2, n+2]$, $L \leqslant L_{\max}$, and $|M| \leqslant L_{\max}$ for $n = 70$ and $L_{\max} = 8$. (The convergence with respect to the basis size will be discussed below.) The spectrum for a pair aligned along the x axis is clearly different from that for the other two orientations. This results because the polarizations of all three lasers (two along the z axis and one along the y axis) are perpendicular to the internuclear axis permitting excitation of $M_x = \pm 3$ states and because the molecular states with small energy shifts have large overlaps with such states. Figure 7(a) gives the resulting excitation strength $I(R)$ integrated over all orientations assuming an isotropic distribution of atom pairs and convoluted with a Gaussian representing the effective laser linewidth in the experiment ($\sim 0.04n^{-3}$ corresponding to $\sim$8 MHz for $n = 310$). The excitation strength is normalized to 1 in the limit of $R \to \infty$, i.e., normalized to the excitation strength for creation of an isolated Rydberg atom. The R dependence of the normalized excitation probabilities for two different values of n ($n = 50$ and 70) are found to agree quite well with each other. This is expected since the pair eigenstates are, as discussed above, approximately scaling invariant. Additionally, the oscillator strengths for excitation of a single atom from a low-lying state to high-n Rydberg states scale as $\sim n^{-3}$ [21], indicating that the pair excitation strength also scales as $\sim n^{-3}$. We define now the blockade radius R_B as the radius where the R-dependent excitation strength $I(R)$ is suppressed by a factor 2, $I(R = R_B) = 0.5$ (indicated by the dotted line in Fig. 7), which results in a scaled blockade radius $R_{B0} \simeq 3$ or $R_B \simeq 3n^{7/3}$ a.u. corresponding to 0.1 mm for $n \sim 300$. For values of $R \lesssim R_B$ the residual excitation strength is distributed over many energy-shifted pair states and the total excitation strength $I(R)$ decreases dramatically, falling

by 80%–90%. In this limit, all pair eigenstates adiabatically connected to the noninteracting $|n,F;n,F\rangle$ pair states are shifted beyond the effective linewidth of the exciting laser. As a result of the high density of states, the excitation of multiple atoms is not completely blockaded within R_B, but rather is strongly suppressed. This finite excitation probability within R_B is mainly due to atom pairs aligned along the x axis (Fig. 6). The energy diagram in the regime where the density of states is high is sensitive to the maximum angular momentum $L_{\max}$ included in the calculations. However, the evaluation of excitation strength involves a convolution with a relatively large laser linewidth ($\sim 0.04n^{-3}$) realized in the experiment rendering fluctuations associated with the choice of $L_{\max}$ relatively small [Fig. 7(b)]. The excitation probability averaged over R within the blockade radius is nearly the same for all values of $L_{\max}$ and the fluctuations in this probability are estimated to be $\sim$10%. As will be shown later, this basis size dependence does not significantly affect evaluation of the Rydberg atom number and the Mandel Q parameter.

IV. ATOMIC MOTION AND BLOCKADE

In a hot atomic beam, the motion of the atoms has a profound influence on the excitation dynamics, especially when correlations between the atoms are introduced via the van der Waals interaction. In the present experiment, atoms are excited via two intermediate states to the target $n \simeq 310$ $^1F_3$ Rydberg state. The excitation rate is typically very small ($\sim 2.8 \times 10^{-4}$ ns^{-1}) and the excitation duration ($\sim$100–800 ns) is shorter than the Rabi flopping period. Therefore, the excitation process can be described by first-order perturbation theory (i.e., Fermi's golden rule) and characterized by the rate γ_0 for a single isolated atom. For $n \sim 300$, the radiative lifetimes of Rydberg states are much longer than the interaction time and therefore can be neglected. Atoms experience, during propagation through the laser focus, spatially varying laser intensities and the spread in arrival times of the atoms in the excitation volume is larger than typical inverse level spacings. Multiple-atom coherences such as the formation of superatoms and the associated enhancement of Rabi frequency are therefore not expected to be important. Moreover, the experimental data represent an ensemble average over a large number of excitation pulses. Therefore, even in the limit of noninteracting atoms, coherences in the excitation process are unlikely to survive. Here we discuss first an analytic rate equation model for a frozen gas and extend it to a hot atomic beam before moving on to present Monte Carlo simulations for the dynamics of excitation and blockade. To quantify blockade effects and atomic correlations, two different mechanisms for allowing excitation of multiple atoms are considered: the finite pair excitation probability within the blockade radius and the motion of atoms out of the excitation volume. These two contributions can be distinguished by their different effects on the Mandel Q parameter.

A. Frozen gas

As a point of reference and to assess the effect of atomic motion in a hot beam, we first consider a gas of N atoms in an excitation volume $V_{\rm ex}$ and neglect their motion. When the linear dimension $V_{\rm ex}^{1/3}$ of the volume is less than the blockade radius $V_{\rm ex}^{1/3} \ll R_B$, excitation of a single Rydberg atom would, for perfect blockade, completely suppress any further Rydberg excitation within the volume. However, in the case of partial blockade where there exists a small but finite excitation rate within R_B (see Fig. 7), the effects of multiple-atom excitation must be included. For simplicity, we assume for the moment that the suppressed excitation rate Γ_0 is constant and independent of R within the blockade radius. In the Monte Carlo simulations presented below these approximations will be avoided. With these simplifications the rate equations that govern the probability $P_i(\tau)$ of finding i Rydberg atoms in the volume $V_{\rm ex}$ at time τ can be written as

$$\begin{aligned}
\frac{d}{d\tau}P_0(\tau) &= -\gamma P_0(\tau),\\
\frac{d}{d\tau}P_1(\tau) &= \gamma P_0(\tau) - \Gamma P_1(\tau),\\
\frac{d}{d\tau}P_i(\tau) &= \Gamma[P_{i-1}(\tau) - P_i(\tau)] \quad (i>1),
\end{aligned} \tag{12}$$

where $\gamma = N\gamma_0$ is the excitation rate for N atoms and $\Gamma = N\Gamma_0$ ($\ll\gamma$) is the suppressed excitation rate. Time $\tau = 0$ corresponds to the turn-on of the exciting laser pulse, i.e., $P_0(\tau=0)=1$ and $P_i(\tau=0)=0$ for $i>0$. Because γ_0 is small, simultaneous excitation of multiple atoms is not included in Eq. (12). For a frozen gas, the number of ground-state atoms decreases as the number i of excitations increases. Therefore, the effective rate Γ should depend on i and decrease with decreasing number of remaining ground-state atoms. However, for a hot beam with continuous replenishment of ground-state atoms in the excitation volume as considered in the following, this dependence can be neglected. We therefore assume for simplicity that Γ is independent of i in Eq. (12) both for the case of a frozen gas and for a beam.

The solution of the rate equations can be found analytically and typical results are shown in Figs. 8(a) and 8(d). As a function of the scaled time $\tau_0 = \gamma\tau$, the time evolution becomes independent of γ (i.e., of the density or the temperature of the atomic beam) and depends only on the parameter $I = \Gamma/\gamma$. The average number of Rydberg atoms [Figs. 8(b) and 8(e)] follows as

$$\langle N_R(\tau)\rangle = \sum_i i\,P_i(\tau) = I\tau_0 + T(\tau_0), \tag{13}$$

where $T(\tau_0) = G(1-e^{-\tau_0})$ with $G = 1-I$. In the short-time limit, Eq. (13) reduces to the unblockaded limit $\langle N_R\rangle \to \gamma\tau = \tau_0$. Indeed, the scaled time corresponds to the expected number of Rydberg atoms in the absence of interaction. In the long-time limit ($\tau_0 > 2$), $P_0(\tau) = e^{-\gamma\tau} \to 0$, meaning that at least one atom is excited and $\langle N_R\rangle \to \Gamma\tau = I\tau_0$. The slope I indicates the degree of blockade. The Mandel Q parameter is a measure of the correlation in the excitation process and is defined such that it is zero for uncorrelated excitations and -1 for a perfectly blockaded ensemble. The solution of the rate equation [Eq. (12)] implies, for the Mandel Q parameter,

$$\begin{aligned}
Q(\tau) &= \frac{\langle N_R^2(\tau)\rangle - \langle N_R(\tau)\rangle^2}{\langle N_R(\tau)\rangle} - 1\\
&= 2Ge^{-\tau_0} - T(\tau_0)\frac{2-T(\tau_0)}{I\tau_0 + T(\tau_0)}.
\end{aligned} \tag{14}$$

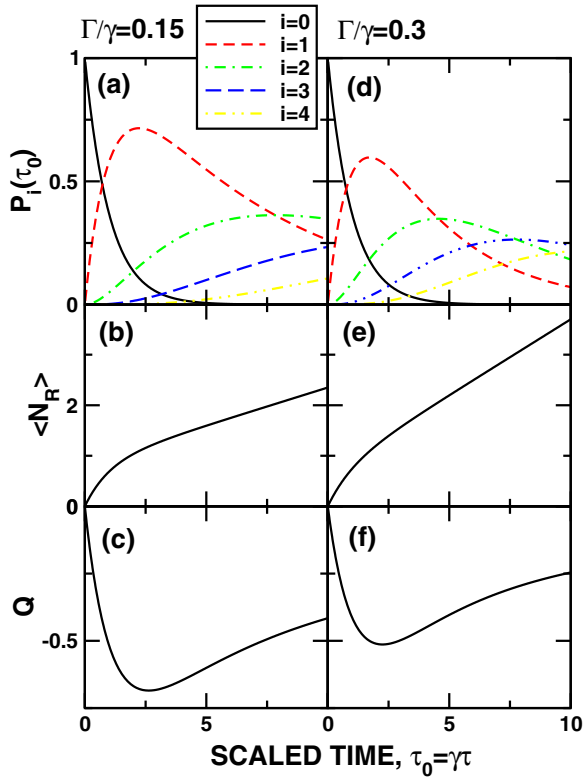

FIG. 8. (a) and (b) Solutions of the rate equations [Eq. (12)] for the probability for finding i atoms in the excitation volume, (b) and (e) the average Rydberg number, and (c) and (f) the Mandel Q parameter. The time axis is scaled by the excitation rate γ and the results are shown for two different values of (a)–(c) $\Gamma/\gamma = 0.15$ and (d)–(f) $\Gamma/\gamma = 0.3$.

Initially, as seen in Figs. 8(c) and 8(f), for small τ, Q decreases linearly

$$Q(\tau) \to -(\gamma - \Gamma)\tau = -G\tau_0, \tag{15}$$

indicating the onset of correlated excitation and, eventually, of blockade. The long-time limit of Eq. (14) would give

$$Q(\tau) \to -G\frac{2-G}{\Gamma\tau + G} = -G\frac{2-G}{I\tau_0 + G}, \tag{16}$$

implying convergence towards zero. Once at least one atom is excited [i.e., $P_0(\tau) \to 0$] and the probability of exciting three or more atoms becomes non-negligible ($\tau_0 > 2.5$), subsequent excitations would become uncorrelated and the Rydberg number distribution $P_i(\tau)$ becomes Poissonian. The latter, however, is an artifact of constant $I = \Gamma/\gamma$ (i.e., independent of internuclear separation R and of the number of Rydberg atoms i). Indeed, as will be discussed below, use of a more realistic I and the effect of atomic motion modify this behavior.

B. Propagating atoms in a hot beam

Atoms in a hot beam propagate with average velocity $v_T = \sqrt{2k_BT/M}$ (~400 m/s in the current experiment), where k_B is the Boltzmann constant, T is the (oven) temperature, and M is the mass of a strontium atom. If the width of the excitation region in the direction of beam propagation is $\mathcal{L}$ (~50 μm), the time it takes for an atom to traverse this region is $\tau_L = \mathcal{L}/v_T \sim$ 120 ns (Fig. 2) and the time it takes for an atom to travel one blockade radius is about twice as long $\tau_B = R_B/v_T \sim 240$ ns. Rydberg atoms that have traveled well beyond the excitation region can still contribute to blockading further excitation. Accordingly, the effective excitation rate for the present beam geometry (Fig. 2) is given by

$$\Gamma_{\text{beam}} = \gamma\mathcal{P}_0 + \Gamma(1 - \mathcal{P}_0), \tag{17}$$

with $\mathcal{P}_0$ the probability of finding no Rydberg atoms inside the blockade radius (but not necessarily inside the excitation region). Assuming now for simplicity that all atoms in the beam move along the x axis with constant speed v_T and the excitation region extends from $x = 0$ to $\mathcal{L}$, the probability $\Delta P_0(x,t)$ of finding no Rydberg atom in the slice $[x, x + dx]$ after exposure to an excitation laser pulse with a duration t obeys the differential equation

$$\frac{d}{dt}\Delta P_0(x,t) = -\gamma_0\rho dx\,\Delta P_0(x,t), \tag{18}$$

where ρ is the number of atoms per unit length and ρdx is the number of atoms in this slice [see Eq. (12)]. In a hot beam, the evolution of a given atom begins at the time t_0 at which it enters the excitation volume at $x = 0$. Therefore, the effective duration τ for which the atom is exposed to the laser field depends on the position x, i.e., $\tau = t - t_0 = x/v_T$. (Only for a frozen gas is $\tau = t$ for all atoms.) The solution of Eq. (18) is given by $\Delta P_0(x,t) = e^{-\gamma_0\rho(t-t_0)dx}$. Consequently, the probability $\mathcal{P}_{\text{in}}$ of finding no Rydberg atom within the entire excitation volume can be estimated as

$$\mathcal{P}_{\text{in}} = \prod_{x=0}^{\mathcal{L}} \Delta P_0(x,t) = \exp\left(-\gamma_0\rho\int_0^{\mathcal{L}}(x/v_T)dx\right) = e^{-\gamma\tau_L/2}, \tag{19}$$

where $\gamma = \gamma_0 N$ and $N = \rho\mathcal{L}$ is the number of atoms in the excitation volume. Extending this estimate to a slice of the beam ($\mathcal{L} < x < \mathcal{L} + \Delta x$) outside the excitation volume but inside the blockade region yields $\mathcal{P}_{\text{out}}(\Delta x) = e^{-\gamma_0\rho\Delta x\tau_L}$. For an atom at position x ($0 < x < \mathcal{L}$) inside the excitation volume, unblockaded excitation is observed when there is no Rydberg atom in the interval $[0, x + R_B]$. The corresponding probability is given by $\mathcal{P}_0(x) = \mathcal{P}_{\text{in}}\mathcal{P}_{\text{out}}(\Delta x = x + R_B - \mathcal{L}) = e^{-(x/\mathcal{L}+b-1/2)\gamma\tau_L}$, with $b = R_B/\mathcal{L}$. Averaged over the entire excitation region, the probability of zero Rydberg atom excitation is

$$\langle\mathcal{P}_0\rangle = \frac{1}{\mathcal{L}}\int_0^{\mathcal{L}}\mathcal{P}_0(x)dx = \frac{1}{\gamma\tau_L}e^{-b\gamma\tau_L}(e^{\gamma\tau_L/2} - e^{-\gamma\tau_L/2}). \tag{20}$$

Using Eq. (20) in Eq. (17) yields the effective rate

$$\Gamma_{\text{beam}} = \gamma\langle\mathcal{P}_0\rangle + \Gamma(1 - \langle\mathcal{P}_0\rangle). \tag{21}$$

Note that, similar to the frozen gas, both the effective probability of zero Rydberg excitation $\langle\mathcal{P}_0\rangle$ and the effective excitation rates Γ_{beam} become invariant under scaling $\tau_{L0} = \gamma\tau_L$ (τ_{L0} is the number of Rydberg excitations during the traversal time of the excitation region in the absence of a blockade). When the blockade region is larger than the excitation volume (i.e., $b > 1$) as in the present experimental setting, $\langle\mathcal{P}_0\rangle$ decreases

monotonically with increasing $\gamma\tau_L$. In the limit $\gamma\tau_L \gg 1$, at least one Rydberg atom is found within the excitation region (i.e., $\langle \mathcal{P}_0 \rangle \sim 0$). Correspondingly, the excitation rate Γ_{beam} approaches Γ. The accumulated number of Rydberg atoms $\langle N_R \rangle$ increases with the laser pulse duration t, leading to $\langle N_R \rangle \sim \Gamma t$. On the other hand, when $\gamma\tau_L < 1$, there is no more than one atom inside the excitation volume. Every time such a Rydberg atom travels beyond the blockade radius, excitation becomes unblockaded and the excitation rate becomes

$$\langle N_R \rangle \sim \Gamma_{\text{beam}} t, \tag{22}$$

with $\Gamma_{\text{beam}} > \Gamma$. Thus the effect of atomic motion becomes observable through $\langle N_R \rangle$ and is more prominent for small $\gamma\tau_L$, i.e., for a low-density beam and/or a short dwell time in the excitation region.

The Mandel Q parameter provides another measure for the effect of atomic motion. While the average number of Rydberg atoms created is cumulative and keeps increasing linearly in the long-time limit [Eq. (22)], the Mandel Q parameter saturates. This is because, once the atom travels beyond the blockade radius, the Rydberg number distribution outside the excitation volume becomes independent of the position x. The consequences for the Mandel Q parameter can be easily deduced from the following consideration: When the same normalized number distribution $f(N_R)$ is found in two partial volumes A and B, the average number of Rydberg atoms is additive

$$\langle N_R \rangle = \sum_{N_R^A, N_R^B} \left(N_R^A + N_R^B\right) f\left(N_R^A\right) f\left(N_R^B\right) = 2\overline{N_R}, \tag{23}$$

where $\overline{N_R}$ indicates the average in a partial volume. Since the second moment behaves analogously,

$$\left\langle N_R^2 \right\rangle = \sum_{N_R^A, N_R^B} \left(N_R^A + N_R^B\right)^2 f\left(N_R^A\right) f\left(N_R^B\right) = 2\overline{N_R^2} + 2\overline{N_R}^2, \tag{24}$$

the Mandel Q parameter in the combined volume

$$Q = \frac{\left\langle N_R^2 \right\rangle - \langle N_R \rangle^2}{\langle N_R \rangle} - 1 = \frac{\overline{N_R^2} - \overline{N_R}^2}{\overline{N_R}} - 1 \tag{25}$$

is identical to that of a partial volume. This can be extended to any number of partial volumes. Therefore, for $t > \tau_B$ the Mandel Q parameter remains unchanged and saturates at the value for $t \simeq \tau_B$. This differs markedly from the behavior of a frozen gas for which Q converges towards zero as $t \to \infty$. While the frozen gas results are independent of temperature in scaled time $t_0 = \gamma t$, the temperature- (or, equivalently, density-) dependent scaled saturation time $(\tau_B)_0 = \gamma\tau_B = N\gamma_0\tau_B$ reveals the temperature dependence in the Mandel Q parameter. This effect of atomic motion is expected to be seen irrespective of the value of $\gamma\tau_L$.

C. Monte Carlo simulation

The excitation dynamics in a propagating atom beam can be more rigorously analyzed using a Monte Carlo method where the fluctuations in the number of ground-state atoms as well as the velocity distributions of the atoms can be accurately accounted for. As will be shown later, the method also allows for the inclusion of a more realistic R-dependent and angle-dependent pair excitation probability (see Figs. 7 and 9). Initially, the positions of N_{tot} atoms are randomly distributed in the volume V of an elliptically shaped cylinder oriented along the direction of propagation of the beam (Fig. 2). Here N_{tot} is determined from the atomic density, which is derived from the vapor pressure [25] at a given oven temperature. A collimated atom beam is simulated by selecting, from a Maxwell-Boltzmann distribution, a subensemble with momenta p_x such that $p_x/p > \cos(\theta_{\text{div}}/2)$, where θ_{div} represents the beam divergence (FWHM). At high temperatures, the kinetic energy of the atoms is much larger than the van der Waals interaction. Therefore, this interaction has a negligible effect on the atomic motion and the atoms are assumed to travel with constant velocities. The cylinder is chosen to be sufficiently long as to ensure that the number of atoms N inside the excitation volume V_{ex} stays nearly constant during the excitation period. The excitation dynamics is simulated using discrete time steps Δt. During a single time step a ground-state atom within the excitation volume $0 < x < \mathcal{L}$ is excited with probability $\gamma_0\Delta t$. Once a single atom is excited, the excitation probability within a blockade radius is reduced to $\Gamma_0\Delta t$. This procedure is iterated for an ensemble of different initial random distributions of the N_{tot} atoms in the excitation volume.

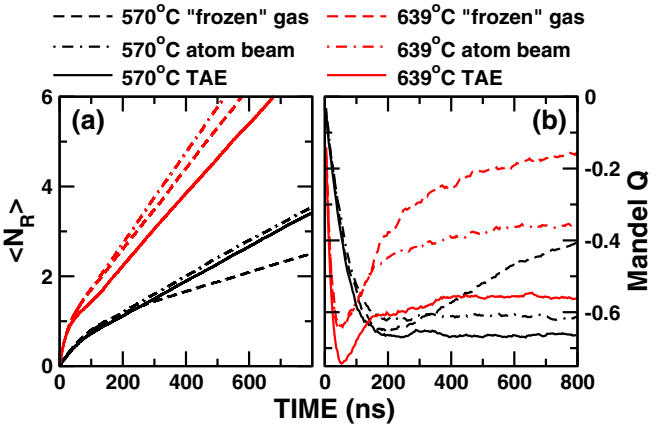

FIG. 9. (a) Calculated average number of Rydberg atoms created and (b) the corresponding Mandel Q parameter. The length of the excitation region is 50 μm. The excitation rate is set to $\gamma_0 = 2.8 \times 10^{-4}$ ns^{-1} and the numbers of atoms are 41 for $T = 570\,^\circ$C (black lines) and 173 for $T = 639\,^\circ$C (red lines). The dashed lines are the calculations for a frozen gas and a blockade radius of 100 μm, the dash-dotted lines are for an atomic beam with a constant $\Gamma = 0.15\gamma$ within the same blockade radius, and the solid lines are for an atomic beam but using the excitation rate $I(\vec{R})$ calculated with the TAE model ($n = 50, L_{\max} = 8$).

Figure 9 shows a comparison between simulations for a frozen gas and an atomic beam with a constant suppressed excitation rate Γ. For simulating a frozen gas, the number density of atoms is taken to be that in the beam, which is determined by the oven temperature, but the velocity is set to zero. Accordingly, at $T = 570\,^\circ$C, $N \sim 41$ atoms are found in the excitation volume, and for $T = 639\,^\circ$C, $\sim$173 atoms. The excitation rate is $\gamma_0 = 2.8 \times 10^{-4}$ ns^{-1} and the blockaded rate is set to $\Gamma_0 = 0.15\gamma_0$ (see Sec. III B). The blockade radius is 100 μm, corresponding to $R_B = 3n^{7/3}$ for $n \simeq 300$. The time for an atom to traverse the excitation region is taken

to be $\tau_L \simeq 120$–125 ns and an atom will travel a distance corresponding to the blockade radius in a time $\tau_B = 240$ ns. In practice, the Monte Carlo simulation for a frozen gas (dashed lines) reproduces the analytical prediction [Eq. (13)]. Here $\langle N_R \rangle$ initially increases linearly, $\sim \gamma t$, and, as blockade sets in, the growth is reduced to $\sim \Gamma t$ [Fig. 9(a)]. The atomic beam simulations (dash-dotted lines) agree well with the frozen gas results for $t < \tau_B$. However, beyond τ_B the excitation rate for the atomic beam is enhanced when compared to the frozen gas, i.e., $\Gamma_{\rm beam} \geqslant \Gamma$ [see Eq. (20)], as the Rydberg atoms travel beyond the blockade radius. This enhancement is more pronounced for the lower temperature because, at the higher temperature and thus higher atomic density, another Rydberg atom is more likely to be excited before a Rydberg atom travels beyond R_B. Here $\langle \mathcal{P}_0 \rangle$ is estimated to be 0.09 for $T = 570\,^\circ$C and 5×10^{-5} for $T = 639\,^\circ$C, implying that for the latter $\Gamma \simeq \Gamma_{\rm beam}$ and the results of the two simulations should approach each other. The remaining difference seen for $T = 639\,^\circ$C in Fig. 9(a), however, is due to the depletion in the number of ground-state atoms in the frozen gas, which modifies the excitation rate $\gamma = N\gamma_0$. The Mandel Q parameter [Fig. 9(b)] also shows good agreement between the frozen gas (dashed lines) and the atomic beam (dash-dotted lines) before it saturates for the atom beam for times $t \simeq 200$ ns, i.e., on the order of τ_B, displaying the effect of atomic motion more clearly than does $\langle N_R \rangle$. The minimum value of Q is temperature independent since a constant ratio $\Gamma/\gamma = 0.15$ is used for the simulations (see Fig. 8). Only for 639 °C is an increase of Q seen after reaching the minimum, implying that the excitation of three or more atoms within the interaction volume becomes non-negligible [Fig. 8(a)]. However, for the lower temperature at most two Rydberg atoms can be excited before one of them travels out of the excitation volume.

D. Position-dependent pair-excitation strength

To obtain more realistic results, the excitation probability $I(R,\theta,\phi)$ calculated using the TAE model is introduced in the Monte Carlo simulation and the sensitivity to the details of the suppressed excitation rate within the blockade radius is examined. Values of $I(\vec{R})$ are plotted in Fig. 6 for selected conditions. To compare the predictions with measured data presented later, the Monte Carlo simulations employ an $I(\vec{R})$ evaluated using a much larger laser linewidth, $\sim 0.04n^{-3}$, than the value used to plot Fig. 6. The residual excitation rate of the ith atom within the blockade radius is evaluated as $\Gamma_0 = I_{\rm corr}(\vec{R}_i)\gamma_0$. When there is only one Rydberg atom (atom j) already present, $\vec{R}_i$ can be uniquely determined as $\vec{R}_i = \vec{R}_{ij}$, with $\vec{R}_{ij}$ defining the relative positions of atoms i and j. As discussed above, for low temperatures at most two Rydberg atoms can be found within the interaction volume. However, for the highest temperature used in the experiment (639 °C) there is a small probability of exciting three (or more) atoms within the blockade radius. Since the evaluation of the excitation strength for multiple-atom eigenstates is very demanding, we approximate this by that for pair eigenstates calculated with the TAE method. We note that simultaneous absorption of multiple photons is not considered in the Monte Carlo model and therefore the excitation strength of, for example, N-atom eigenstates implies the probability

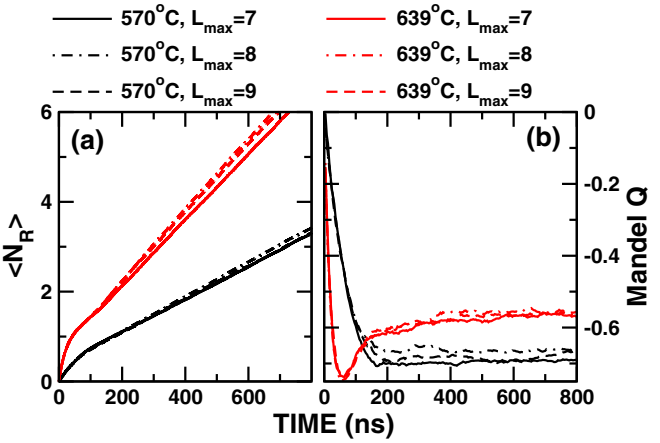

FIG. 10. (a) Calculated average number of Rydberg atoms created and (b) the corresponding Mandel Q parameter. The calculations are for an atomic beam using the excitation rate $I(\vec{R})$. Each line corresponds to the excitation rate $I(\vec{R})$ calculated using the TAE model with a different basis size: $n = 50$ with $L_{\rm max} = 7$ (solid line), $L_{\rm max} = 8$ (dash-dotted line), and $L_{\rm max} = 9$ (dashed line).

of exciting the Nth atom when the other $N-1$ atoms are already excited. We evaluate an "average" position $\vec{R}_i$ of the already excited $N-1$ Rydberg atoms and the suppressed rate is evaluated using $I(\vec{R}_i)$ calculated for the pair eigenstates. The average distance R_i is evaluated as a power mean, i.e.,

$$R_i = \left(\sum_{j \in \rm Ryd} R_{ij}^{-\lambda} \right)^{-1/\lambda}, \tag{26}$$

where the summation extends over $N-1$ Rydberg atoms. The polar angles θ and ϕ of $\vec{R}_i$ are taken from those of the nearest Rydberg atom. In the following simulations we choose the power $\lambda = 6$ taken from the R dependence of the van der Waals interaction. We have also tested other values between $\lambda = 3$ and 6, but the results are found to be insensitive to the value of λ. Whereas the inclusion of the $\vec{R}$ dependence of the excitation rate has little influence for lower temperatures (Fig. 9), it has a significant influence at higher temperatures since the pair excitation of atoms at smaller separations becomes more accessible due to the higher density of atoms. The average number of Rydberg atoms $\langle N_R \rangle$ becomes smaller in the long-time limit when using $I(\vec{R})$ than when using a constant $\Gamma = 0.15\gamma$. This implies that the pair eigenstates are excited below $R_0 < 2$ for which $I(\vec{R}) < 0.15$ (Fig. 7). Correspondingly, the Mandel Q parameter becomes smaller [Fig. 9(b)] due to the stronger blockade effect. The uncertainties in the excitation strength seen at small R [Fig. 7(b)] do not substantially affect the behavior of $\langle N_R \rangle$ and Q (Fig. 10). This is because the average of $I(\vec{R})$ over distance R largely cancels basis-size-induced fluctuation effects.

V. COMPARISON BETWEEN EXPERIMENT AND SIMULATION

Figure 11(a) shows the mean number of Rydberg atoms $\langle N_R \rangle$ excited as a function of the scaled time $t_0 = \gamma t$ for a

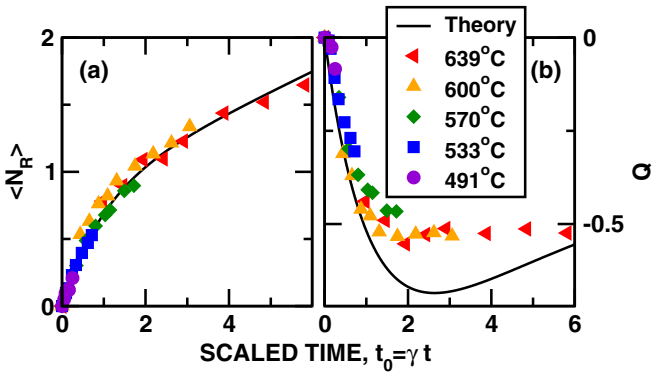

FIG. 11. (a) Mean number $\langle N_R \rangle$ and (b) the Mandel Q value of $n \sim 310$ Rydberg atoms excited as a function of the duration of the AOM drive pulse for the oven operating temperatures T indicated. For comparison, the analytical predictions of the rate equations for a frozen gas [Eq. (12)] with $I = \Gamma/\gamma = 0.15$ for $\langle N_R \rangle$ and Q are also given. The pulse duration is scaled as $t_0 = \gamma t$.

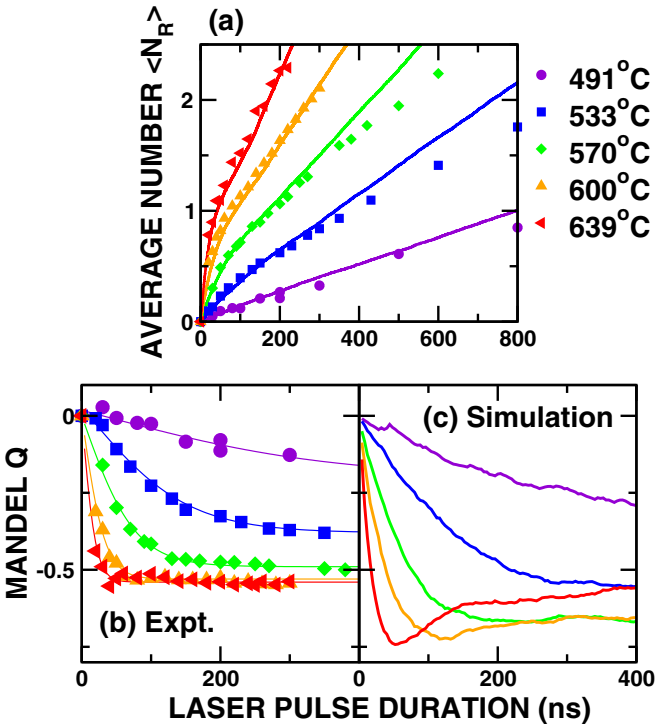

FIG. 12. (a) Mean number $\langle N_R \rangle$ of $n \sim 310$ Rydberg atoms excited as a function of the duration of the AOM drive pulse for the oven operating temperatures T indicated. The symbols are the measured data and the lines are the Monte Carlo simulation results. The corresponding Q values are presented in (b) for the measured data and in (c) for the Monte Carlo results.

number of different oven operating temperatures, i.e., beam densities, and a fixed 893-nm laser power of 1 W. (The results presented in Figs. 11–13 are corrected for the detection efficiency η; $\langle N_R \rangle$ and Q both scale as $1/\eta$.) Preliminary measurements of the transmission characteristics of the AOM showed that for drive pulse widths $t_d < 40$ ns the optical output pulse width remained almost constant (at ~40 ns) but its amplitude decreased at a rate such that the energy in the transmitted pulse remained proportional to t_d. For values of $t_d > 40$ ns the optical output pulse width scales with t_d. For comparing to experiment, the theoretical model assumes a constant amplitude pulse with a duration $t = t_d$ and a uniform laser intensity over the $(1/e^2)$ width of the laser beam. We have tested a more realistic distribution of laser intensity in both space and time, but this did not lead to any significant differences. This is because the degree of blockade $\Gamma/\gamma = I(\vec{R})$ is independent of laser intensity and consequently the time evolutions of $\langle N_R \rangle$ and Q are affected little. We note that the laser intensity does not significantly affect the linewidth dominated by Doppler broadening and therefore does not modify the degree of blockade.

First we compare the measured data with the analytical solution for a frozen gas (Fig. 11). To minimize the effect of atomic motion, only the measured data with pulse duration $t < 150$ ns are used. The pulse duration is scaled by $t_0 = N\gamma_0 t$ with $\gamma_0 = 2.8 \times 10^{-4}$ ns^{-1} and N is derived from the vapor pressure of strontium. As predicted, $\langle N_R \rangle$ and Q are nearly independent of temperature when expressed as a function of scaled time. At early times $t_0 < 1$ (i.e., when at most one Rydberg atom is expected in the excitation volume), $\langle N_R \rangle$ scales as $\sim t_0$, indicating that the excitation rate before blockade sets in is given by $\gamma = N\gamma_0$ and is proportional to the beam density. After blockade sets in for $t_0 > 2$, the analytical solution converging to $\langle N_R \rangle \sim (\Gamma/\gamma)t_0$ agrees well with the measured data, confirming that the suppressed rate is about $\Gamma = 0.15\gamma$. However, the measured Q values are less than predicted by the frozen gas model, indicating that it overestimates the effect of blockade.

For more realistic estimates, $\langle N_R \rangle$ and Q are calculated using the Monte Carlo method [Fig. 12(a)]. The excitation rate γ_0 is taken from the measured value 2.8×10^{-4} ns^{-1} and the suppressed excitation rate from $I(\vec{R})$ calculated with the TAE model (Fig. 6). The average Rydberg number $\langle N_R \rangle$ is well reproduced by the simulations even for $t > 200$ ns, for which the effect of atomic motion becomes significant [Fig. 9(a)]. The Mandel Q parameter [Figs. 12(b) and 12(c)], on the other hand, is underestimated by 30% in the Monte Carlo simulation. This discrepancy starts appearing even for $t_0 = \gamma t < 2$ (see Fig. 11), i.e., when the excitation of at most two atoms is expected. The effect of blockade appears much smaller in the measured Q values as opposed to $\langle N_R \rangle$. Indeed, $\Gamma \simeq 0.3\gamma$ would yield a minimum Q value of $\simeq -0.5$. Uncertainties in the oven temperature and in the excitation volume do not strongly modify the ratio Γ/γ and therefore may not be the main reason for the present discrepancy. The current calculations may underestimate Γ (Fig. 10). A more accurate calculation including contributions beyond the Born-Oppenheimer approximation and the effective line broadening for short pulses may be necessary to explain this discrepancy. However, the correction in Γ should be limited so that the good agreement in $\langle N_R \rangle$ is maintained. Another potential source of the discrepancy might be uncertainties in the detection efficiency η. Even allowing for some uncertainty in η, however, no single value of η was found that leads to agreement in both Q and $\langle N_R \rangle$. For high temperatures 600 °C and 639 °C, a small increase of Q is seen after reaching the minimum.

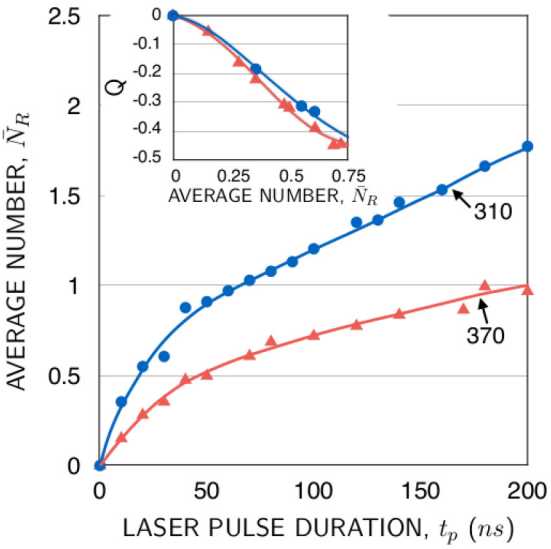

FIG. 13. Mean number $\langle N_R \rangle$ of $n \sim 310$ and $n \sim 370$ Rydberg atoms excited under identical experimental conditions as a function of AOM drive pulse width t_d (see the text). The corresponding Q values are shown in the inset as a function of $\langle N_R \rangle$.

This is the regime where the excitation of three or more atoms becomes non-negligible. The approximation used for multiple-atom excitation [Eq. (26)] is a perturbative treatment and valid when only one Rydberg atom is nearby. However, at higher temperatures, there is a non-negligible probability of finding multiple Rydberg atoms in close proximity and the perturbative treatment may break down. Since the measured data display almost no increase in Q, this indicates that the excitation of multiple atoms is suppressed more than predicted by the theoretical model.

We have also verified experimentally the n scaling of partial blockade by exciting $n \sim 310$ and $n \sim 370$ states under otherwise identical experimental conditions (Fig. 13). As expected, the two data sets display many of the same characteristics. Moving to higher n reduces the Rydberg excitation rate by a factor of $\sim(310/370)^3 \simeq 0.6$. In consequence, larger laser pulse widths are required to create $\langle N_R \rangle \sim 1$ Rydberg atoms, suggesting that atomic motions will be more important. However, this is offset by the fact that, for the same laser linewidth, the blockade radius should be increased by a factor $\sim(370/310)^{11/6} \simeq 1.4$, requiring that a Rydberg atom created in the excitation volume must travel a larger distance before the excitation of a further Rydberg atom can occur. The asymptotic excitation rate Γ_{beam} [Eq. (20)] can be evaluated as 4.6×10^{-3} ns^{-1} for $n = 310$ and, by scaling γ and R_B, for $n = 370$ can be estimated as 2.8×10^{-3} ns^{-1}, in accord with the measured data, which approach the long-time limit $\Gamma_{\text{beam}} t$. For small values of $\langle N_R \rangle$, i.e., for short laser pulses $t_d \lesssim 100$ ns, the Mandel Q parameter is expected to be proportional to the mean Rydberg number $\langle N_R \rangle$, i.e.,

$$Q = -\frac{\gamma - \Gamma}{\gamma} \langle N_R \rangle \tag{27}$$

[see Eqs. (13) and (15)]. Since both γ and Γ scale as n^{-3}, this relation is n-scaling invariant. Indeed, as shown by the inset in Fig. 13, the measured Q values are nearly identical functions of $\langle N_R \rangle$. With increasing $\langle N_R \rangle$, however, small differences start to appear.

VI. CONCLUSION

The present work demonstrates that with careful control of stray fields and laser polarizations, strong blockade effects can be observed in a high-temperature, $T \sim 600\,^\circ$C, atom beam even when using very-high-n atoms with relatively high L (in the present case, $L = 3$). While the direct calculation of Rydberg-Rydberg interactions and of pair-excitation strengths for very high-n ($n \gg 100$) is challenging, scaling invariance provides a useful theoretical tool to overcome this problem. Rydberg-Rydberg interactions remove the degeneracy of pair states involving high-L Rydberg atoms. At small internuclear distances the oscillator strength is distributed over many sublevels. Since for high n the laser linewidth becomes effectively large ($\sim$4% of the energy spacing between adjacent n levels, n^{-3}), the probability of excitation of an interacting pair, while small, can be non-negligible. This suppressed, but nonzero, pair excitation probability provides a means for exciting multiple Rydberg atoms, which affects the correlation of Rydberg excitation in the long-time limit. Concurrently, the motion of atoms in a high-temperature beam reduces the effects of blockade because Rydberg atoms, once created, may leave the excitation volume. This motion, however, does not strongly modify the correlation and the Mandel Q parameter is found to eventually saturate.

A further extension of the present study of Rydberg blockade in a hot beam will involve multiple excitation volumes. Estimating the probability of exciting a single Rydberg atom in the excitation volume, the probability of exciting one, and only one, Rydberg atom in each of two well-separated Rydberg excitation volumes becomes sizable ($\sim$0.6). This might be further enhanced [14] by reducing the excitation volume and/or by reducing its width along the x axis so as to have fewer pairs of atoms aligned along the x axis (see Fig. 6). Furthermore, improvements in detection efficiency promise better discrimination against events in which fewer than, or more than, two Rydberg atoms are created. Thus blockade in separate excitation volumes promises creation (and identification) of Rydberg atom pairs with well-defined initial separations. This, coupled with manipulation of the wave functions of the Rydberg pairs using tailored electric field pulses [26], opens opportunities for detailed time-resolved studies of Rydberg-Rydberg interactions.

ACKNOWLEDGMENTS

This research was supported by the NSF under Grants No. PHY-1301773 and No. PHY-1600059, by the Robert A. Welch Foundation under Grant No. C-0734, by the FWF (Austria) under Grant No. P23359-N16, and by SFB-049-NextLite. The Vienna scientific cluster (VSC) was used for the calculations.

[1] D. Tong, S. M. Farooqi, J. Stanojevic, S. Krishnan, Y. P. Zhang, R. Côté, E. E. Eyler, and P. L. Gould, Phys. Rev. Lett. **93**, 063001 (2004).
[2] K. Singer, M. Reetz-Lamour, T. Amthor, L. G. Marcassa, and M. Weidemuller, Phys. Rev. Lett. **93**, 163001 (2004).
[3] D. Møller, L. B. Madsen, and K. Mølmer, Phys. Rev. Lett. **100**, 170504 (2008).
[4] T. Wilk, A. Gaëtan, C. Evellin, J. Wolters, Y. Miroshnychenko, P. Grangier, and A. Browaeys, Phys. Rev. Lett. **104**, 010502 (2010).
[5] X. L. Zhang, L. Isenhower, A. T. Gill, T. G. Walker, and M. Saffman, Phys. Rev. A **82**, 030306 (2010).
[6] D. Jaksch, J. I. Cirac, P. Zoller, S. L. Rolston, R. Côté, and M. D. Lukin, Phys. Rev. Lett. **85**, 2208 (2000).
[7] M. Müller, I. Lesanovsky, H. Weimer, H. P. Büchler, and P. Zoller, Phys. Rev. Lett. **102**, 170502 (2009).
[8] L. Isenhower, E. Urban, X. L. Zhang, A. T. Gill, T. Henage, T. A. Johnson, T. G. Walker, and M. Saffman, Phys. Rev. Lett. **104**, 010503 (2010).
[9] A. Gaëtan, Y. Miroshnychenko, T. Wilk, A. Chotia, M. Viteau, D. Comparat, P. Pillet, A. Browaeys, and P. Grangier, Nat. Phys. **5**, 115 (2009).
[10] Y. O. Dudin, L. Li, F. Bariani, and A. Kuzmich, Nat. Phys. **8**, 790 (2012).
[11] E. Urban, T. A. Johnson, T. Henage, L. Isenhower, D. D. Yavuz, T. G. Walker, and M. Saffman, Nat. Phys. **5**, 110 (2009).
[12] A. M. Hankin, Y.-Y. Jau, L. P. Parazzoli, C. W. Chou, D. J. Armstrong, A. J. Landahl, and G. W. Biedermann, Phys. Rev. A **89**, 033416 (2014).
[13] D. Barredo, S. Ravets, H. Labuhn, L. Béguin, A. Vernier, F. Nogrette, T. Lahaye, and A. Browaeys, Phys. Rev. Lett. **112**, 183002 (2014).
[14] X. Zhang, F. B. Dunning, S. Yoshida, and J. Burgdörfer, Phys. Rev. A **92**, 051402 (2015).
[15] D. Maxwell, D. J. Szwer, D. Paredes-Barato, H. Busche, J. D. Pritchard, A. Gauguet, K. J. Weatherill, M. P. A. Jones, and C. S. Adams, Phys. Rev. Lett. **110**, 103001 (2013).
[16] C. Tresp, C. Zimmer, I. Mirgorodskiy, H. Gorniaczyk, A. Paris-Mandoki, and S. Hofferberth, Phys. Rev. Lett. **117**, 223001 (2016).
[17] L. Mandel, Phys. Rev. Lett. **49**, 136 (1982).
[18] S. Ye, X. Zhang, F. B. Dunning, S. Yoshida, M. Hiller, and J. Burgdörfer, Phys. Rev. A **90**, 013401 (2014).
[19] M. Hiller, S. Yoshida, J. Burgdörfer, S. Ye, X. Zhang, and F. B. Dunning, Phys. Rev. A **89**, 023426 (2014).
[20] C. L. Vaillant, M. P. A. Jones, and R. M. Potvliege, J. Phys. B **45**, 135004 (2012).
[21] S. Ye, X. Zhang, T. C. Killian, F. B. Dunning, M. Hiller, S. Yoshida, S. Nagele, and J. Burgdörfer, Phys. Rev. A **88**, 043430 (2013).
[22] S. Nagele, R. Pazourek, J. Feist, and J. Burgdörfer, Phys. Rev. A **85**, 033401 (2012).
[23] T. F. Gallagher, K. A. Safinya, F. Gounand, J. F. Delpech, W. Sandner, and R. Kachru, Phys. Rev. A **25**, 1905 (1982).
[24] K. Singer, J. Stanojevic, M. Weidemuller, and R. Cote, J. Phys. B **38**, S295 (2005).
[25] G. D. Maria and V. Piacente, J. Chem. Therm. **6**, 1 (1974).
[26] F. B. Dunning, J. J. Mestayer, C. O. Reinhold, S. Yoshida, and J. Burgdörfer, J. Phys. B **42**, 022001 (2009).